Naval Research Laboratory
Washington, DC 20375-5000



NRL Memorandum Report 6667

# Numerical Simulations of the Structure of Supersonic Shear Layers

B. FAROUK,* E. S. ORAN, AND K. KAILASANATH

*Laboratory for Computational Physics and Fluid Dynamics*
*Washington, DC 20375*

**Mechanical Engineering and Mechanics Department*
*Drexel University*
*Philadelphia, PA 19104*



July 20, 1990

# REPORT DOCUMENTATION PAGE

Form Approved
OMB No. 0704-0188



| 1. AGENCY USE ONLY (Leave blank) | 2. REPORT DATE | 3. REPORT TYPE AND DATES COVERED |
|---|---|---|
| | 1990 July 20 | |

**4. TITLE AND SUBTITLE**

Numerical Simulations of the Structure of Supersonic Shear Layers

**5. FUNDING NUMBERS**

PE - ONR
PR - ONR
TA - RR0110943
WU - 44153000

**6. AUTHOR(S)**

B. Farouk,* E. S. Oran and K. Kailasanath

**7. PERFORMING ORGANIZATION NAME(S) AND ADDRESS(ES)**

Naval Research Laboratory
Washington, DC 20365-5000

**8. PERFORMING ORGANIZATION REPORT NUMBER**

NRL Memorandum Report 6667

**9. SPONSORING/MONITORING AGENCY NAME(S) AND ADDRESS(ES)**

Office of Naval Research
800 N. Quincy Street
Arlington, VA 22217-5000

**10. SPONSORING/MONITORING AGENCY REPORT NUMBER**

**11. SUPPLEMENTARY NOTES**

*Mechanical Engineering and Mechanics Department
Drexel University, Philadelphia, PA 19104

**12a. DISTRIBUTION/AVAILABILITY STATEMENT**

Approved for public release; distribution unlimited.

**12b. DISTRIBUTION CODE**

**13. ABSTRACT** *(Maximum 200 words)*

Time-dependent two-dimensional numerical calculations were performed to study the mixing characteristics of unforced, planar, confined shear layers formed by two parallel streams of air that come into contact after passing over a splitter plate. The evolution of the shear layer was examined by systematically varying the velocities, densities, and the static pressures of the two streams that come into contact at the trailing edge of the plate. At least one of the streams was always supersonic. For the range of the parameters studied, the supersonic shear layers show some organization, albeit less coherent than their subsonic counterparts. The most amplified frequency, obtained by Fourier analysis of the velocity and pressure fluctuations, depends on the effective inlet momentum thickness. Convective Mach numbers of the streams corresponding to each side of the shear layer were found to be quite different. The simulations indicate that the single convective Mach number as derived from an isentropic model is not sufficient to characterize the mixing behavior when the velocity, pressure, and density ratios are changed independently.

| 14. SUBJECT TERMS | 15. NUMBER OF PAGES |
|---|---|
| Numerical simulations, Supersonic shear layers | 41 |
| | 16. PRICE CODE |

| 17. SECURITY CLASSIFICATION OF REPORT | 18. SECURITY CLASSIFICATION OF THIS PAGE | 19. SECURITY CLASSIFICATION OF ABSTRACT | 20. LIMITATION OF ABSTRACT |
|---|---|---|---|
| UNCLASSIFIED | UNCLASSIFIED | UNCLASSIFIED | UL |

## CONTENTS



# NUMERICAL SIMULATIONS FO THE STRUCTURE OF SUPERSONIC SHEAR LAYERS

## I. INTRODUCTION

Supersonic shear layers are inherently more stable than their subsonic counterparts, and this results in the practical consequence that there is less mixing. Adequate mixing in supersonic flows is, however, an essential requirement for propulsion devices designed to provide chemical reactions, and heat release in supersonic streams of air and fuel. For this reason, an understanding of the behavior of supersonic shear layers and jets is a necessary prerequisite to setting criteria for the control of mixing and energy release in supersonic flows.

This paper presents a numerical investigation of the role of selected inlet flow variables on mixing and stability in a bounded, unforced supersonic shear layer. More specifically, two-dimensional time-dependent simulations of the mixing of two supersonic parallel streams of gas (initially separated by a splitter plate) are performed to determine the effects of the density, velocity, and pressure differences between the streams. The paper reports and compares the relative qualitative differences in mixing that occurs and the types of coherent structures that are formed.

In these simulations, we have taken particular advantage of the fact that computations can extend the work of analysis into the nonlinear regime for even broader ranges of parameters, and yet the flow conditions are still idealized and easily specified and varied. Physical properties can be measured and shocks and other flow structures can be detected, all of which are difficult to observe experimentally. As with idealized analytical solutions and basic fluid experiments, the purpose is to gain insight into some of the fundamental parameters controlling the behavior of the flow and present guidelines for when to expect more mixing and for choice of sensible but very expensive three-dimensional computations.

Manuscript approved April 17, 1990.

## II. BACKGROUND

Subsonic shear layers have attracted investigators for many years. Brown and Roshko [2] made a fundamental breakthrough by discovering that shear layers form discrete large-scale structures. These structures can become relatively large and roll up in a coherent manner that greatly increases the mixing surface. It was later shown that the growth rate of the layer is governed by the pairing of these structures. Subsonic jets and shear layers are naturally unstable and usually lead to this large-scale mixing. The higher the Mach number, the longer it takes for a jet or a shear layer to become unstable, thus reducing the amount of mixing in a given time and distance. At high Mach numbers, the mixing is substantially reduced. With growing interest in supersonic propulsion systems and hypersonic airbreathing vehicles, there is an immediate need to understand the basic mechanisms causing the reduced mixing and for overcoming the apparent limits. The physics of supersonic shear layers is presently under intense research[3-8].

In subsonic shear layers, the basic method of relating the different properties of the streams is to normalize with respect to the high velocity stream. In supersonic mixing, however, large changes in the density ratio can cause the low Mach number stream to have a greater velocity than the high Mach number stream. The basis for normalization is thus not clearly defined for supersonic shear layers. Recent studies[2-8] have attempted to use the 'convective Mach number' as a normalization parameter in one way or the other. The definitions of the upper and lower convective Mach numbers (for equal pressure cases) are[3]

$$M_{c,1} = \frac{U_1 - U_c}{a_1}; \qquad M_{c,2} = \frac{U_c - U_2}{a_2} \qquad (1)$$

where $U_1$ and $U_2$ are the free stream velocities of the upper and lower streams and $U_c$ is the convective velocity of the structures (assumed to be constant) . The quantities $a_1$ and $a_2$ are the sonic velocities of the two streams at the inlet condition. For the overexpanded (faster stream at a

lower pressure) and underexpanded cases, the inlet parameters are replaced by the conditions of the two streams where they reach static pressure equilibrium after undergoing rarefaction and compression .

The relation between $M_{c,1}$ and $M_{c,2}$ is traditionally obtained by requiring that the total pressure of the two streams in the convective frame be equal[3]. This originates from a well-known subsonic flow argument, which state that there exists a stagnation point between two structures that must be stable, so that the pressures at that point must balance. Equating the stagnation pressures of the two streams produces an estimate of the convective velocity of the structure.The above argument was subsequently applied to supersonic flows by Papamoschou and Roshko[3], who assumed that the flow comes to rest isentropically at the stagnation point. Hence, no shock-wave losses were accounted for. If the upper and lower streams both have the same ratio of specific heats, then the velocity of the convected disturbances is given by

$$U_c = \frac{a_1 U_2 + a_2 U_1}{a_1 + a_2} \qquad (2)$$

and there is just one convective Mach number ,

$$M_c = M_{c,1} = M_{c,2}$$

Recent measurements of Papamoschou[9] have, however, shown that the convective Mach numbers corresponding to each side of a shear layer ($M_{c,1}$ and $M_{c,2}$) are very different, thus contradicting the above isentropic model of structures which predicts that they are equal or very close.

Spark Schlieren photographs[3-4] have shown that the growth rate of supersonic shear layers is significantly less than that of incompressible shear layers layers with the same velocity and density ratios between two mixing streams. The drastic reduction in growth rate has been correlated to $M_c$ as defined above. The experimental measurements[3] show that the ratio of the

growth rate of a supersonic shear layer to the growth rate of an incompressible shear layer, (with the same velocity and density ratios), decreases as $M_c$ increases. This growth rate decreases rapidly in the range $M_c$ ~ 0.4 - 0.5. The relative reduction again levels off as $M_c$ exceeds unity. Recent measurements in supersonic shear layers[4-6] also confirm this observation. Linear inviscid stability analysis has shown[7] a similar correlation between the ratio of maximum growth rates of stability waves of supersonic and incompressible shear layers and $M_c$ based on a frame of reference traveling with the instability waves. For very small values of $M_c$, the reported ratio of the growth rate of a supersonic shear layer to the growth rate of an incompressible shear layer is near unity.

Experimental studies of the details of the mixing layer in supersonic shear layers are difficult as the mixing layer is complex when the streams are supersonic[3-4]. In addition, the properties of supersonic shear layers are sensitive to small variations in the density ratio of the two streams. This in turn can affect the optical diagnostic systems used to characterize the shear layers. In such physical systems, numerical computations often provide missing information and behavior trends. They have an advantage in that there are no interference effects present due to measurement probes. In addition, they can simulate situations where the flow conditions are difficult or expensive to achieve in the laboratory. However, as with any tool, there are important limitations to what the simulations can do. The validity of the results depends on the computational domain chosen, the particular algorithm used to solve the model equations and its implementation of the initial and boundary conditions, the particular computer, and even the interpretation of the output data.

Numerical simulations have been and are currently a powerful tool for investigating the evolution of subsonic shear layers[10-12]. Due to the presence of complicated shock structures and sharp gradients, accurate simulations of the supersonic shear layers warrant algorithms with minimal numerical diffusion. Recently Guirguis et al.[1] have demonstrated the applicability of

numerical simulations to the study of fundamental processes in time-dependent two-dimensional supersonic shear layers. The Flux-Corrected Transport (FCT) algorithm was used to study the mixing and structure in supersonic shear layers. Soestrino et al.[13] studied the evolution of instabilities and the physical processes associated with turbulent mixing of temporally supersonic shear layers, i.e., shear layers with periodic boundary conditions in the flow directions. A second-order total variation diminishing (TVD) algorithm was used. Numerical simulations of shear layers in open domains were recently carried out by Lele[14]. In this case, the two streams were matched in static pressure but had different densities. The spatially evolving simulations presented were forced at the inflow by adding a small normal velocity disturbance at the most unstable frequency and its first two subharmonics. In the temporally evolving simulations, small amplitude incompressible disturbances were added to the initial tangent hyperbolic flow profile. The behavior of a plane free shear layer was studied by Tang et al.[15]. A second-order ADI procedure as well as a modified McCormack algorithm were used to obtain the solutions. Small-amplitude oscillations in the normal velocity were found to grow as they convected downstream.

This work, following Guirguis et al.[1], is a first attempt to do a systematic numerical parameter study of unforced and confined supersonic shear layers. The procedure is to select a base case and vary the parameters around this case in a systematic way. The base case consists of two (equal pressure) parallel streams of supersonic gas at inlet Mach numbers of 4.0 and 1.5, respectively, flowing in a chamber bounded on the sides. The density, velocity, and pressure in the two streams are varied so that equal pressure, underexpanded, and overexpanded systems are considered. In the calculations presented here, however, the effective momentum thickness is generally held fixed.

The present work extends the previous work in several ways. First, the parameters were systematically varied to look for the regimes of enhanced mixing. The evolution of the major

physical quantities in an unforced system is presented and these are used to analyze the dynamics of the flow and the mixing characteristics. Two diagnostics, flow visualization and fourier analysis, were used in this study to help analyze the computed results.The convective velocities $M_{c,1}$ and $M_{c,2}$ are directly measured from the predictions and compared to the isentropic value. Since the same medium (air) was considered for both streams, for equal pressure cases, the density variation of the streams was caused by temperature differences.

## III. THE NUMERICAL MODEL

The physical system we simulate, shown schematically in Fig. 1, is a confined mixing layer formed by two streams of gases initially separated by a splitter plate. The flow domain is bounded by two perfectly smooth parallel walls. The splitter plate is not included in the computational domain and its trailing edge forms the left boundary of the computational domain. For supersonic essentially inviscid flow calculations, this does not introduce significant errors as there is no feedback of information upstream. The initially laminar streams have a top-hat axial velocity profile at the trailing edge of the splitter plate and this profile is held constant during the computations. The calculations are unforced in the sense that no external frequency is imposed on the flow. These are idealized initial conditions since most laboratory tunnel flows are not laminar at the Mach numbers considered in this paper .

For the calculations reported, the inflowing upper stream is always supersonic and at a higher velocity than the inflowing lower stream. The lower stream can be either supersonic or subsonic . By analogy to supersonic jets, an underexpanded shear layer is defined as the one in which the pressure of the faster stream is higher at the entrance than that of the slower stream and vice versa for overexpanded shear layers. Underexpanded, equal-pressure, and overexpanded shear layers were considered. As shown in Figure 1, properties of the faster stream are denoted by $_1$

subscript 1, and the slower flow by 2.

The numerical model used to carry out the simulations consists of the two-dimensional, time-dependent inviscid conservation equations of mass density , momentum and energy density for an ideal gas:

$$\frac{\partial \rho}{\partial t} = -\nabla.(\rho \mathbf{V}) \tag{3}$$

$$\frac{\partial (\rho \mathbf{V})}{\partial t} = -\nabla.(\rho \mathbf{V}\mathbf{V}) - \nabla P \tag{4}$$

$$\frac{\partial E}{\partial t} = -\nabla.(E\,\mathbf{V}) - \nabla.P\mathbf{V} \tag{5}$$

Here $E = P/(\gamma - 1) + (1/2)\rho V^2$ is the total energy and V (where $\mathbf{V} = iU + jV$), P, $\rho$ and $\gamma$ are the fluid velocity vector, pressure, total mass density, and the ratio of the specific heats, respectively. To compute the mixing (as a result of convection), each of the two streams is convected separately, allowing us to calculate the mixing in any given computational cell. This was done by considering the conservation equations for individual species densities for the upper and lower streams.

The equations are solved using the nonlinear, high-order, explicit, compressible finite-difference FCT algorithm (Boris and Book[16]). Through a two-step predictor corrector scheme, FCT ensures that all conserved quantities remain monotonic and positive. First, it modifies the linear properties of a high order algorithm by adding diffusion during convective transport to prevent dispersive ripples from arising. The added diffusion is then removed in an antidiffusion phase of the integration cycle. Hence these calculations maintain the high order of accuracy without requiring artificial viscosity to stabilize the algorithm. The algorithm has been extensively tested and used in the last ten years (see, for example bibliography in Oran and Boris[17]) to predict a wide

variety of reactive and nonreactive flows. The explicit FCT algorithm was used (Oran et al.[18]) to investigate the properties of condensational instabilities in solar and astrophysical plasmas. Growth rates, decay rates and oscillation frequencies of the perturbations determined from the linear analysis were in excellent agreement with the simulations. In addition, the FCT algorithm has been used for the analysis of a variety of plasma and fluid dynamic instability problems[19,20]. Employing the FCT algorithm, Grinstein et al.[21-22] calculated the vortex dynamics and asymmetric mixing in compressible subsonic plane and axisymmetric shear layers in both two and three dimensions. Also using this algorithm, Kailasanath et al.[23] have calculated the behavior of cold and chemically reacting axisymmetric confined jets. The present calculations were carried out using the code LCPFCT which uses the most recent one-dimensional version of Flux-Corrected Transport technique with fourth-order accurate phases and minimum residual diffusion. A timestep-splitting technique is used to couple the two dimensions. The calculations are vectorized to take full advantage of the architecture of the CRAY-XMP supercomputer used for the calculations.

No explicit subgrid turbulence model was included. However, there is an effective filter for high frequencies which is part of the nonlinearity of the FCT algorithm. The filter does not affect the large-scale structures, but ensures that wavelengths smaller than a few computational cells are numerically diffused. Thus, provided that the computational grid is fine enough to resolve the large-scale features of the flow, the residual numerical viscosity of the algorithm mimics the behavior of physical viscosity at high Reynolds number by damping small-scale structures on the order of a few computational cells. There are essentially no viscous effects at scales greater than four or five computational cells.

A 25 cm x 3 cm ( X x Y ) computational domain was considered for the majority of the cases studied. The splitter plate was located symmetrically between the confining walls. The two streams are ideal gases (air) with constant specific heats. Inflow and outflow boundary conditions

must be used to represent the effects of the outside world on the computational domain. Ideally, such boundary conditions would not allow unphysical reflections or wave absorption at the boundaries of the computational domain. Imposing such boundary conditions is difficult numerically and is currently the topic of a great deal of numerical analysis research.This difficulty is most evident in numerical simulations of subsonic flows, but it is not such a major problem in supersonic flows. The inlet conditions of the dependent variables were specified. Zero-gradient outflow conditions (at X = L) were used for all variables. The top and bottom of the computational region (Y = 0 and H) are perfectly reflecting hard walls. A 191 x 61 (X x Y ) uniform grid was used for most of the calculations reported. The mesh was uniform in order to ensure that downstream and deflected structures were well resolved. A series of calculations were performed where the inlet Mach numbers, velocity , pressures and densities of the two streams at the inlet were systematically varied. Extended domains with the same grid density , 40 cm x 3 cm and 40 cm x 5 cm and denser-grid calculations (382 x 122 and 382 x 61) on the same 25 cm x 3 cm domain were also performed for a specific base case. The Courant number was held at 0.5 to insure numerical stability and to resolve the time evolution properly. This condition was based on a velocity equal to sound speed plus flow speed characteristic of the faster stream.

The boundary layers and the actual velocity profiles on the splitter plate are important parameters since they provide a characteristic transverse length scale for the shear-layer instability. Since different experimental set-ups have different boundary layers and velocity profiles developing on the splitter plate the characteristic length scale $\theta_o$ (the initial momentum thickness) can vary from one set of experiments to another. Our calculations were started with a step-function velocity profile (with a slope $\Delta U/\Delta Y$ where $\Delta U = U_1 - U_2$ and $\Delta Y$ is the cell width in the Y direction) across the shear layer, i.e., an infinitesimally thin vortex sheet spanning the whole domain, from the trailing edge of the splitter plate up to the right boundary. These profiles smooth out during the initial timesteps and relax to a shear-layer profile with an effective initial momentum thickness $\theta_o'$.

As found in experiments, $\theta_o'$ can vary among different simulations performed for example, using different algorithms. Therefore it is important to characterize the relevant lengthscales in either calculations or experiments. Earlier calculations using the approach adopted in this paper have shown that a step-profile for the inlet velocity produces an estimate of $\theta_o'$ as one or two cell-width in the cross stream direction[9]. Our present calculations also support this observation, which means that we can determine an effective initial momentum thickness by setting the grid spacing.

The small perturbation which initiates the transition from laminar to transitional flow occurs at the first time step of the calculations. The perturbation generates small pressure gradients and diffuses vorticity at the shear layer, near the edge of the splitter plate. Due to the smoothing of the initial step-function profile, the initially uniform pressure field (for equal pressure cases) develops a small gradient across the thickening shear layer in the region close to the edge of the splitter plate where the free streams meet. This disturbance moves downstream as the integration proceeds, generating the transverse flows which trigger the instability.

The numerical simulations predict values of the density, momentum, energy and number-density ratio for each of the computational cells as a function of time. The evolution of the flow is shown through sequences of contours of number-density ratio, where

$$R = N_1 / (N_1 + N_2)$$

The $N_1$ and $N_2$ are the number densities corresponding to the top and bottom inflowing streams. The value of R varies between 0 and 1; a value of 0 corresponds to 100% of the bottom stream and a value of 1 corresponds to 100% of the top stream.

Kailasanath et al.[23] have shown that the peaks in velocity- and pressure-fluctuations spectra taken at fixed locations can be related to the organization and coherence in the flow. The fluctuations at a given location reflect the local passage of large structures as well as information

about events at other locations of the flow transmitted by sound waves, such as vortex mergings that generate fluctuations in compressible flows. A strong narrow spectral line usually indicates that a structure passes the location at a very regular interval. We have therefore performed fourier analysis of pressure and velocity fluctuations at selected positions in the computational domain to help determine the organization and coherence in the flow.

## IV. RESULTS and DISCUSSION

The computations performed are divided into three broad categories:

1. Both streams are at the same pressure and are supersonic as they pass the tip of the splitter plate. Calculations were performed by either keeping the density uniform and varying the velocity ratios or by maintaining the velocity ratio constant and varying the density ratios.
2. Both streams are at the same temperature and supersonic at the inlet, but the pressures of the two streams at the inlet are different. Both underexpanded and overexpanded cases were considered.
3. Both streams are at the same pressure and temperature, but the upper stream is supersonic and the lower stream is subsonic.

The convective Mach number, $M_c$, as obtained by equation (2) was computed for each case and are reported with the inlet parameters.

### 1.) Equal-Pressure Streams

#### a. Uniform density

The convective Mach number and the velocity ratios were systematically varied by decreasing the Mach number of the lower stream, $M_2$, while keeping the Mach number of the upper stream, $M_1$, constant. Conditions for the base case are given in Table I. For these conditions, the value of $M_c$ is directly proportional to $(M_1 - M_2)$, so that $M_c = 1.25$.

Figure 2 shows the contours of the mixing ratio R within the computational domain at a sequence of times corresponding to 8.6 μs intervals or 50 time steps, at a range of time well past the initial stages of the development of the flow in the calculations. The shear layer initially becomes unstable at approximately 9 cm from the tip of the splitter plate. Subsequently coherent structures develop and move downstream. The paths of some of these organized structures in the figure show that there is merging indicating that the convective velocities of all the structures are not the same. The convective velocities of these structures (as computed from Figure 2) significantly differ from the (theoretical) value of $M_c = 1.25$. For instance, the convective velocity of a typical structure, the one at the left undergoing merging with a smaller structure, was $11.6 \times 10^4$ cm/s which gives $M_{c,1} = 0.67$ and $M_{c,2} = 1.83$. As expected, this does not agree with predictions of the the isentropic model. The above results are, however, consistent with the recent experimental observations by Papamoschou[9].

Figure 3 shows the density contours of the flow field at the end of time step 4000. The density field remains uniform until the shear layer becomes unstable. A system of oblique shock waves is observed attached to the large structures in the lower half of the domain where the computed $M_{c,2} = 1.83$. The evolution of the flowfield shown in Figure 2 can be related to the fourier analysis of the pressure and velocity fluctuations observed at specific downstream locations in the computational domain. In Figure 4 we show the spectra of the transverse velocity and pressure fluctuations at the point (18.75 cm, 2.0 cm), indicated by an "X" in Figure 1. The location was chosen after sample calculations were made and regions with distinctive structures were identified. Both the pressure and velocity fluctuations show a dominant frequency of 30 kHz, corresponding to the passage of the structures shown in Figure 2. The fourier analyses do not show strong specific subharmonics signifying that the passing structures do not merge in any clearly synchronized way.

Table I. Base case conditions

| | 1 | 2 |
|---|---|---|
| $\rho$ | $1.17 \times 10^{-3}$ gm/cm$^3$ | $1.17 \times 10^{-3}$ gm/cm$^3$ |
| T | 300 K | 300 K |
| P | $1.01 \times 10^6$ dynes/cm$^2$ | $1.01 \times 10^6$ dynes/cm$^3$ |
| U | $13.95 \times 10^4$ cm/s | $5.22 \times 10^4$ cm/s |
| M | 4.0 | 1.5 |

Figure 5 compares contours of the mixing ratio R at timestep 4000 for calculations in which $M_2$ was gradually increased, $M_2$ = 2.0, 3.0, and 3.5. The value of $M_1$ and all other conditions were kept the same as the base case, which resulted in $M_c$ = 1.0, 0.5, and 0.25 and velocity ratios $U_1/U_2$ = 2.0, 1.33, and 1.13, respectively. The contours of R show that as the velocity ratio decreases, the shear layer spreads less and becomes unstable further downstream, a result also seen in subsonic shear layers . The spectra of the pressure and velocity fluctuations become noisier as $M_c$ and the velocity ratio decrease with a proliferation of peaks between 40 kHz and 80 kHz range in the spectrum.

Calculations were also carried out with $M_1$ decreased to 2.5 and $M_2$ remaining the same as in the base case. This corresponds to a velocity ratio $U_1/U_2$ = 1.66 and $M_c$ = 0.5. The contours of R, shown in Figure 6 at the end of timestep 4000 , show a very stable shear layer with no

convective mixing. The slight spread in the shear layer is caused by the small though nonzero residual numerical diffusion associated with the finite-difference scheme. Figures 5(b) and 5(c) show that the shear layer becomes unstable in the same computational domain for cases where the velocity ratio $U_1/U_2$ is lower than 1.66. In particular, the value of $M_c$ is same for cases shown in Figures 5(b) and 6. However, $M_1 = 4.0$ and $M_2 = 3.0$ in Figure 5(b) while the corresponding values in Figure 6 are 2.5 and 1.5 respectively. Since the calculations were carried out without any forcing, the pressure fluctuations are unable to trigger the Kelvin-Helmholtz instability within the length of the computational domain in Figure 6. Guirguis et al.[1] have shown earlier that an unforced supersonic shear layer, that appears stable in a short computational domain, may eventually become unstable further downstream.

To study the flow in a longer domain, the following cases were considered with the inlet conditions identical to the base case. First, the computations were carried out on a domain with dimensions of 40 cm x 3 cm with a 300 x 61 grid. This gave the same grid density as in the base case but the domain is 15 cm longer. Figure 7 depict the contours of R for this case at the end of time step 4000. Here the growth of the naturally unstable shear layer was obstructed downstream by the walls. The domain dimensions were then increased to 40 cm x 5 cm with a 300 x 101 grid to keep the same grid density. Figure 8 shows contours of the mixing ratio R within the computational domain at a sequence of times for the extended domain. As in Figure 2, the frames in Figure 8 are 8.6 $\mu$s apart which corresponds to 50 timestep intervals. As in the base case, the instability is triggered near 9 cm . However, the mixing increases substantially in the extended length of the domain. The slight differences in the contours in the first 25 cm of Figure 8 and Figure 2 are attributed to the different heights of the confining chambers, which in turn impose slightly different acoustic properties on the system. The computed velocities for $M_{c,1}$ and $M_{c,2}$ (for a typical structure) were close to those found from Figure 2. These calculations also show that in this study, the location of the outflow boundary has little effect on the flow field predictions

upstream.

For simulations performed by *nonlinear monotone* methods such as FCT, the residual numerical diffusion is finite but very low. Hence for simulations that do not include an explicit model for physical viscosity or for which the physical viscosity is less than the numerical viscosity, the effective Reynolds numbers for various sized structures in the flow are determined by the mesh size. Because of this inherent nonlinearity of the method, the effective Reynolds number varies according to the size of the structure resolved relative to the mesh spacing. For example if a structure is resolved by twenty computational cells, the effective Reynolds number is very high and the flow is essentially inviscid for this structure. If the structure is resolved by three cells, the effective Reynolds number is low and the structure can be dissipated. The nonlinearity of the method means that the progression to increased effective Reynolds number is faster than linear. Thus when mesh size is decreased, small-scale structures of the flow are resolved as long as the physical viscosity is less than the numerical viscosity. For larger mesh size, the small scales are filtered out. In order to study the effects of grid size and the inlet velocity profile on the solutions, the base case calculations were done with different computational grids, viz. 382 x 61 (twice as fine in the X direction) and 382 x 122 (twice as fine in both X and Y directions). Contours of mixing ratio R at the end of timestep 1000 is shown in Figures 9(a) and 9(b) for the base case ( 191 x 61) and for the 382 x 61 grid respectively. For these two cases, the inlet velocity profile ( and hence $\theta_o'$ ) is identical as the cross stream cell width is the same. Though the essential large scale features shown in the two figures are similar, more small-scale structures are found in Figure 9(b) due to the finer grid size in the X direction only. Figure 9(c) shows the mixing contours obtained with a grid of 382 x 122 at the same physical time and precisely the same inlet velocity profile considered in Figures 9(a) and 9(b). Due to the doubling of the grid in the Y direction, $\Delta Y$ is half the size used in the above cases. The inlet velocity profile was, however, spread linearly across two cross stream cells so that it was identical to those applied for Figures 9(a) and 9(b). The agreement between the

predictions shown in Figures 9(a) and 9(c) is good. As the solution progressed in time, the similarities of the above predictions became less evident due to the effective filtering of high frequencies. The filter does not affect the large-scale structures, but ensures that wavelengths smaller than a few computational cells are numerically diffused. It is, however, evident that the shape of the inlet profile plays a key role in the development of the instability and for the present calculations, the large-scale structures are essentially grid independent.

Predictions were also obtained with the 382 x 122 grid where the inlet velocity profile was across one cross stream cell only. Figures 10(a) and 10(b) compare the contours of R with the denser grid (with the above inlet velocity profile) to those of R for the base case at the same physical time. Note that because $\theta_o'$ is halved, the physics of the two flows is different. In the denser-grid case, the mixing instability occurs at a shorter downstream distance, about 4.5 cm from the trailing edge of the splitter plate, compared to the base-case prediction where the instability is triggered near 9 cm. However, there is a physical similarity in the two solutions: the flow structures in the first half of Figure 10(a) look very much like those in Figure 10(b), only half the size. The shedding frequencies computed by the fourier analyses of the pressure and velocity fluctuations (as shown in Figure 11) were approximately twice the corresponding shedding frequencies predicted in the base case. The similarity in the solution of equations is consistent with the fact that $\theta_o'$ was reduced by reducing the cross stream cell width.

b. Constant Velocity Ratios

For the equal-pressure cases, the density ratio was varied by changing the temperature ratios of the two streams but keeping the velocity ratios constant. The velocities of the upper and lower streams were $U_1 = 8.71 \times 10^4$ cm/s, $U_2 = 5.22 \times 10^4$ cm/s respectively, so that $U_1/U_2 = 1.66$. Results were obtained for two situations, one in which the faster stream is four times

denser than the slower stream ($\rho_1/\rho_2 = 4.0$ and $T_1/T_2 = 1/4$) and the other in which the faster stream is four times lighter than the slower stream ($\rho_1/\rho_2 = 1/4$ and $T_1/T_2 = 4.0$). For the case where the faster fluid is denser, $M_1 = 5.0$ and $M_2 = 1.5$, and for the case where the faster fluid is lighter, $M_1 = 2.5$ and $M_2 = 3.0$. It is interesting to note that for both of these cases, $M_c = 0.67$.

The instantaneous contours of R for the two cases described above are shown in Figures 12(a) and 12(b) at the end of time step 4000. Due to the temperature changes in the streams due to density differences, the time steps must be slightly different to satisfy the imposed Courant number condition for stability and accuracy. The case where the faster fluid is lighter (hotter), is found to be stable and no convective mixing occurs. However, significant mixing occurs when the faster fluid is denser (colder) and here the contours of R show organized structures.

It has been shown from linear theory that the effect of temperature differential is different for subsonic disturbances as opposed to supersonic disturbances (Gropengiesser[24], Ragab and Wu[7]). Brown and Roshko[2] investigated the density effects in subsonic turbulent mixing layers. According to this study, when the faster stream is denser ($U_1/U_2 = \sqrt{7}$ and $\rho_1/\rho_2 = 7$), decreased spreading of the shear layer was observed compared to the case where the faster stream is slightly lighter than the slower stream ($U_1/U_2 = \sqrt{7}$ and $\rho_1/\rho_2 = 0.965$). Our present results for the supersonic shear layer and the observations by Brown and Roshko for the subsonic shear layer are thus consistent and agree with the predictions by the linear theory.

2. Underexpanded and Overexpanded Cases

When the pressures of the two streams are different, the high-pressure stream expands through a rarefaction fan centered at the tip of the splitter plate while the low-pressure stream is

compressed to the same pressure through an oblique shock wave also attached to the tip of the splitter plate. The actual flow parameters affecting the properties of the shear layer are the values ahead of these waves. The conditions ahead of the shock or rarefaction waves that form for the overexpanded and underexpanded cases will be denoted by 1' and 2' for the top and the bottom streams, respectively, as was done in Guirguis et al.[1].

Figure 13 shows the density contours in the computational domain at a time step 4000 for an underexpanded case where $P_1 = 2.02 \times 10^6$ dynes/cm$^2$, $P_2 = 1.01 \times 10^6$ dynes/cm$^2$ and $\rho_1 = 2.34 \times 10^{-3}$ gm/cm$^3$, $\rho_2 = 1.17 \times 10^{-3}$ gm/cm$^3$. The remaining parameters are identical to those shown in Table 1. For this case, the temperatures of the two stream at the tip of the splitter plate are equal (300 K). As a result of the pressure difference, the shear layer turns 4.5$^o$ towards the lower wall. The higher pressure flow on top expands through a rarefaction fan centered at the tip of the splitter plate to a pressure $P_1' = 1.232 \times 10^6$ dynes/cm$^2$, while the lower pressure, slower flow compresses through an oblique shock wave to the same pressure $P_2' = 1.232 \times 10^6$ dynes/cm$^2$. Ahead of the rarefaction fan, $M_1' = 4.38$, $T_1' = 263.2$ K and $\rho_1' = 1.676 \times 10^{-3}$ gm/cm$^3$. Ahead of the shock wave, $M_2' = 1.373$, $T_2' = 308$ K and $\rho_2' = 1.32 \times 10^{-3}$ gm/cm$^3$. The (isentropic) convective Mach number at the above conditions is $M_c = 1.36$. The density contours illustrate the interaction between the reflected rarefaction and shock waves at the walls and the shear layer. The oblique shock wave starting at the splitter plate reflects from the bottom wall. When the shock intersects the shear layer, it is partially transmitted and partially reflected due to the higher density of the top layer. This produces a perturbation that triggers the Kelvin-Helmholtz instability. Further complex interactions of the walls with transmitted and reflected shocks occur in the downstream flow.

Figure 14 shows the contours of R at a sequence of times. As in Figure 2, each frame in Figure 14 is 8.6 μs apart which corresponds to intervals of 50 time steps. The time sequences of

R exhibit enhanced mixing and organization of the structures compared to those shown in Figure 2. This is perhaps due to the presence of shocks in the vicinity of the splitter plate which perturbs the shear layer. The process of merging is indicated by the two dashed lines coming together at step 4250. The computed values of $M_{c,1}$ and $M_{c,2}$ for the structure at the left undergoing pairing in Figure 13 are 0.918 and 2.22 respectively as opposed to the theoretical value of $M_c$ = 1.36. Since $M_{c,2}$ > 1.0, oblique shocks waves are thus found in the lower half of the computational domain in Figure 13.

In Figure 15 we show the spectra of the transverse pressure fluctuations at 18.75 cm from the left boundary and 2.0 cm from the lower wall. Comparing the results to those in Figure 4(b) show that a second strong peak appears in the pressure fluctuation spectrum reflecting the more organized merging process seen in Figure 14.

In order to investigate further the effects of underexpansion and overexpansion on the mixing behavior, the inlet parameters for the case shown in Figure 6 (that exhibited little convective mixing) was considered. Both underexpanded ($P_1/P_2$ = 2.0, $\rho_1/\rho_2$ = 2.0) and overexpanded cases ($P_1/P_2$ = 0.5, $\rho_1/\rho_2$ = 0.5) were considered. For both cases, $M_1$ = 2.5 and $M_2$ = 1.5 and $T_1$ = $T_2$ = 300 K. Figures 16(a) and 16(b) show the contours of R at a given time (timestep 4000) for the underexpanded and the overexpanded cases. For the underexpanded case, the shear-layer deflection is 6.0° while in the overexpanded cases, the deflection is about 5°. These cases show that both underexpansion and overexpansion enhance mixing compared to the equal-pressure case shown in Figure 6. However, convective mixing in the overexpanded case is significantly less than the underexpanded case where the inlet temperatures of the two streams are the same. Both cases show organized large-scale mixing and the structures appear similar in shape to those observed in subsonic shear layers. The shear layer becomes unstable near 15 cm from the trailing edge (for the underexpanded case) of the splitter plate. The velocity and density ratios in the shear layer

immediately ahead of the shock and the rarefaction waves are $U_1'/U_2' = 1.96$ and $\rho_1'/\rho_2' = 1.26$ for the underexpanded case and $U_1'/U_2' = 1.45$ and $\rho_1'/\rho_2' = 0.81$ for the overexpanded case.

## 3. Supersonic-Subsonic Interactions

A number of experimental studies have been performed where a supersonic flow meets subsonic flow at the trailing edge of a splitter plate [3, 4]. In this section, the results of a limited computational study carried out on confined shear layers formed by a supersonic and a subsonic stream are reported. The mathematical formulation and the boundary conditions were identical to those reported in an earlier section. The computational domain and the grid sizes were also similar to those used in the base case reported earlier. Two cases were considered for which where the inlet Mach number of the slower, subsonic stream was held at $M_2 = 0.5$. For the supersonic stream, inlet Mach number values of $M_1 = 1.5$ and 2.5 were used. For both streams, inlet pressure and density were $1.01 \times 10^6$ dynes/cm$^2$ and $1.17 \times 10^{-3}$ gm/cm$^3$, respectively. The convective Mach number, $M_c$ for the first case is 0.5 and for the second case is 1.0.

Figure 17 shows the contours of R within the computational domain at a sequence of times 17.2 μs apart corresponding to 50 timestep intervals for the case where $M_1 = 1.5$. The shear layer remains stable for most of the length of the computational domain and then rolls up in a fashion characteristic of subsonic shear layers. It is of particular interest to compare these results to those shown in Figures 5(b) and 6. In each case, $M_c = 0.5$ and density ratios are the same. The velocity ratios ($U_1/U_2$) are 1.37 in Figure 5(b), 1.66 in Figure 6 and 3.0 for the present case. The computed values of $M_{c,1}$ and $M_{c,2}$ for a typical large structure (as shown by the dashed line in Figure 16) is found to be 0.31 and 1.05 respectively. Thus even for supersonic-subsonic interactions, the convective Mach numbers for the upper and lower stream are quite different from

the theoretical value.

In Figure 18 we show the spectra of the pressure fluctuations for this case again at (18.75 cm, 2.0 cm). Prominent peaks are observed near 20 kHz and in addition, there is a subharmonic indicating pairing . Note that for cases where both streams are supersonic, the peaks are clustered near 30 kHz. The difference is attributed to the existence of the subsonic stream and acoustic interactions. As the Mach number difference and the convective Mach number are increased ( $M_1 = 2.5$ and $M_2 = 0.5$) , the point of instability is found to shift further downstream. The mixing between the two streams also decreases within the length of the domain considered. The structures in this case did not exhibit features similar to those found in subsonic shear layers. Further work (with improved outflow boundary conditions) needs to be done for characterizing subsonic-supersonic shear layer.

## V. CONCLUSIONS

This paper has presented numerical simulations of time-dependent two-dimensional unforced supersonic shear layers for a splitter-plate geometry. The calculations were performed using the Eulerian explicit Flux-Corrected Transport algorithm to solve the convective transport problem. The natural instability of supersonic shear layer was investigated by systematically varying the velocity, pressure, and density ratios of the two streams while keeping the effective inlet momentum thickness constant .

The supersonic shear layers were found to be naturally unstable and to have well-defined large structures. The organization and coherence of the structures deteriorates as the absolute Mach number of the streams increases and the Mach number difference between the stream decreases. For

equal pressure and equal density streams, the mixing depends on the Mach number difference as well as the Mach number of the faster stream. In this case, mixing decreased with decreasing convective Mach number, $M_c$.

The most amplified frequency obtained by the fourier analysis of the velocity and pressure fluctuations depends on the effective inlet momentum thickness ( the cell-width in the cross-stream direction). For the inviscid calculations presented with a step-function inlet velocity profile, the cell width in the cross-stream direction provides a length scale similar to the initial momentum thickness of the shear layer. The most-amplified frequency did not depend on other parameters like pressure and density ratios in the shear layer.

The mixing behavior of the unforced supersonic shear layer could not be uniquely described by the convective Mach number as derived from the isentropic model[3] . Even with the same velocity and density ratios, different shear layers with the same convective Mach number show different natural instability characteristics. Convective velocities $M_{c,1}$ and $M_{c,2}$ were computed from the predictions and were compared to the (isentropic) theoretical value : they were found to be very different. This finding is in agreement with the recent experimental observations by Papamoschou[9]. The present results and the experimental observations[9] contradict the current isentropic model of the structures which predicts $M_{c,1}$ and $M_{c,2}$ to be equal or very close.

Differences in pressure across a supersonic shear layer also enhance the convective mixing. When the walls are close, shock waves originating at the tip of the splitter plate reflect from the nearest wall and intersect the shear layer before it goes unstable naturally. For equal-temperature streams with the same Mach numbers, underexpansion causes better mixing than overexpansion .

For equal-pressure streams, mixing is enhanced when the faster stream is denser (cooler). This was found by simulating equal-pressure shear layers with identical velocity ratios but different density and temperature ratios. It is interesting to note that Brown and Roshko[2] discovered the opposite trend for subsonic mixing layers. This difference for subsonic and supersonic shear layer has been also confirmed by the linear theory[7,24].

## ACKNOWLEDGMENTS

The computations reported in this paper were carried out during June - August 1988 at the Naval Research Laboratory, Washington, D. C., where one of the authors (BF) served as an ASEE/NAVY Summer Faculty Research Associate. This work is sponsored by the Naval Research Laboratory through the Office of Naval Research.

## REFERENCES

1. R. H. Guirguis, F. F. Grinstein, T. R. Young, E. S. Oran, K. Kailasanath and J. P. Boris, AIAA 87-0373 (1987).

2. G. L. Brown and A. Roshko, J. Fluid Mech. **64**, 775 (1974).

3. D. Papamoschou and A. Roshko, AIAA 86-0162 (1986) also J. Fluid Mech. **197**, 453 (1988).

4. N. Chinzei, G. Mauya, T. Komuro, A. Murakami and K. Kuduo, Phys. Fluids, **29**, 1345 (1986).

5. M. Samimy and G. S. Elliott, AIAA 88-3045A (1988).

6. N. L. Messersmith, S. G. Goebel, W. H. Frantz, E. A. Krammer, J. P. Renie, J. C. Dutton and H. Krier, AIAA 88-0702 (1988).

7. S. A. Ragab and J. L. Wu, AIAA 87-1418 (1987).

8. J. P. Drummond and M. Y. Hussaini, AIAA 87-1325 (1987).

9. D. Papamoschou, AIAA 89-0126 (1989).

10. F. F. Grinstein, E. S. Oran and J. P. Boris, J. Fluid Mech. **165**, 201 (1986).

11. J. Riley and R. W. Metcalfe, AIAA 80-0274 (1980).

12. A. Ghoneim and K. K. Ng, AIAA 86-0056 (1986).

13. M. Soestrino, S. Eberhardt, J. J. Riley and P. McMurty, AIAA 88-3676.

14. K. Lele, AIAA 89-0374 (1989).

15. W. Tang, N. Komerath and L. Sankar, AIAA 89-0376 (1989).

16. J. P. Boris and D. L. Book, Methods in Comp. Phys., **16**, Academic Press, 85 (1976).

17. E. S. Oran and J. P. Boris, Numerical Simulation of Reactive Flow, Elsevier, (1987).

18. E. S. Oran, J. T. Mariska and J. P. Boris, and Astrophysical Journal, **254**, 349 (1982).

19 J. M. Picone and J. P. Boris, Physics of Fluids, **26**, 365 (1983).

20. J. Grun, M. H. Emery, C. K. Manka, T. N. Lee, E. A. Mclain, A. Mostovych, J. Stamper, S. E. Bodner, S. P. Obenschain and R. P. Rippin, Phys. Rev. Letters, **58**, 2672 (1987).

21. F. F. Grinstein, E. S. Oran and J. P. Boris, AIAA J., **25**, 92 (1987).

22. F. F. Grinstein, E. S. Oran and F. Hussain, AIAA 88-0042 (1988).

23. K. Kailasanath, J. H. Gardner, E. S. Oran and J. P. Boris AIAA 88-0339 (1988).

24. H. Gropengeisser, NASA TTF-12-78, (1970).

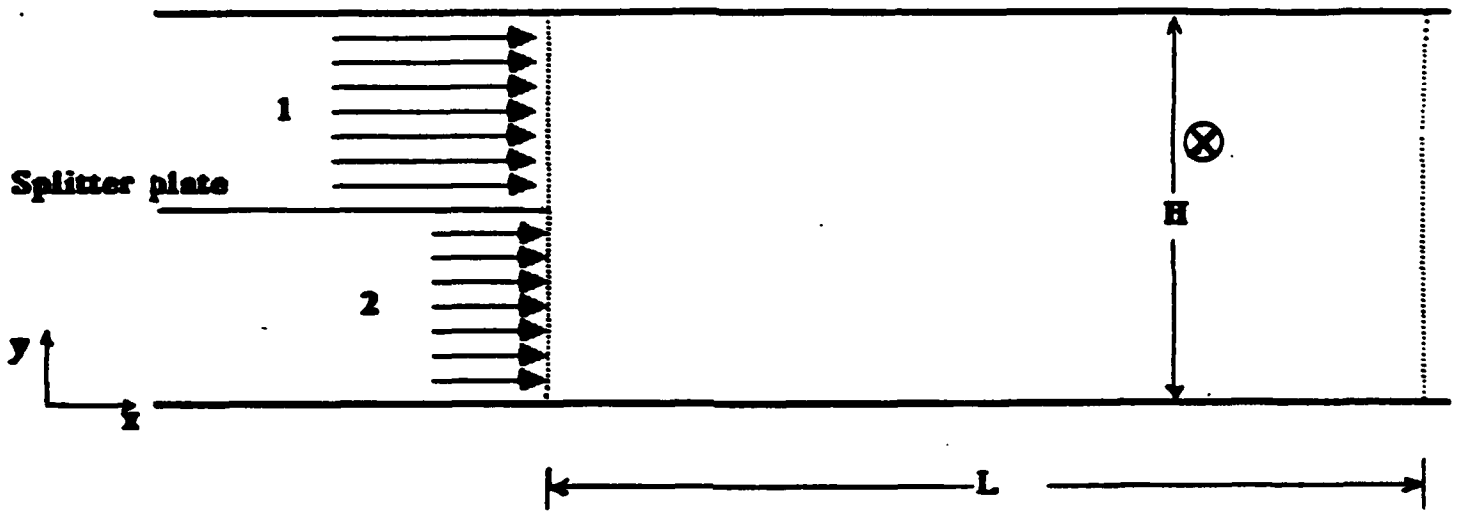


Figure 1. Schematic of the problem geometry

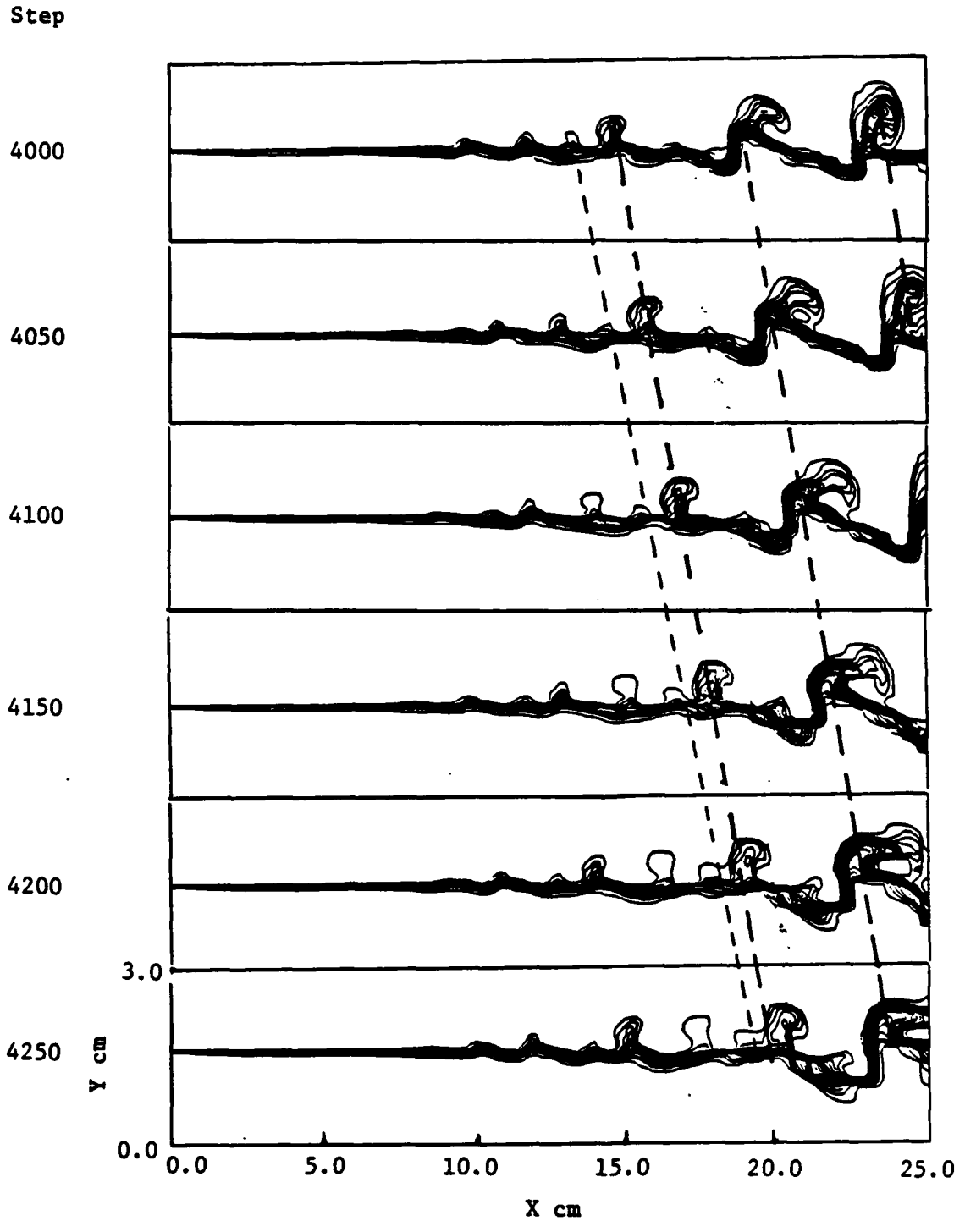


Figure 2. Contours of mixing ratio R from 0.01 to 0.99 at a sequence of time steps for the base case.

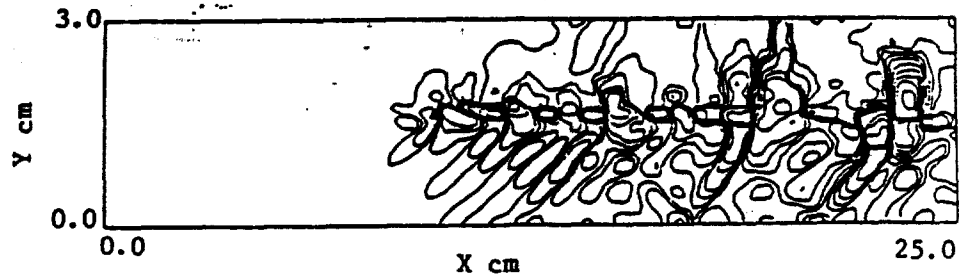


Figure 3. Density contours from $2.15 \times 10^{-4}$ gm/cm$^3$ to $2.15 \times 10^{-3}$ gm/cm$^3$ for the base case at the end of time step 4000.

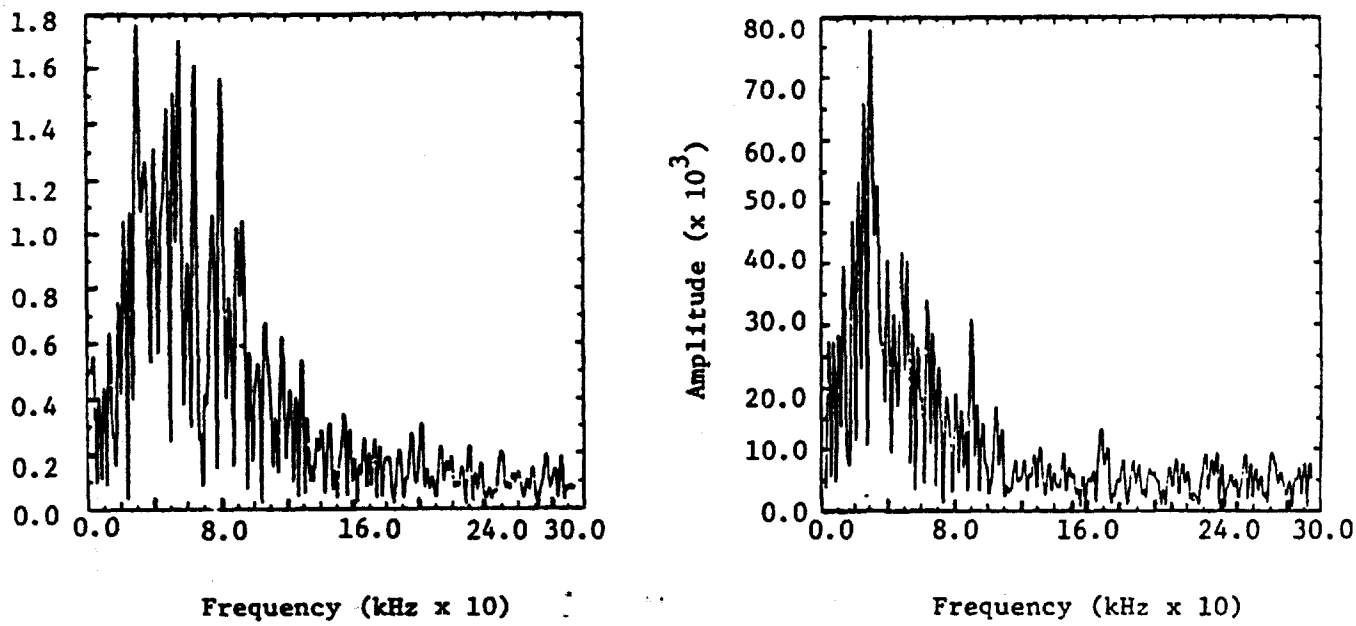


(a) Transverse velocity fluctuations

(b) Pressure fluctuations

Figure 4. Frequency spectra in the shear layer for the base case at the location 18.75 cm (X), 2.0 cm (Y)

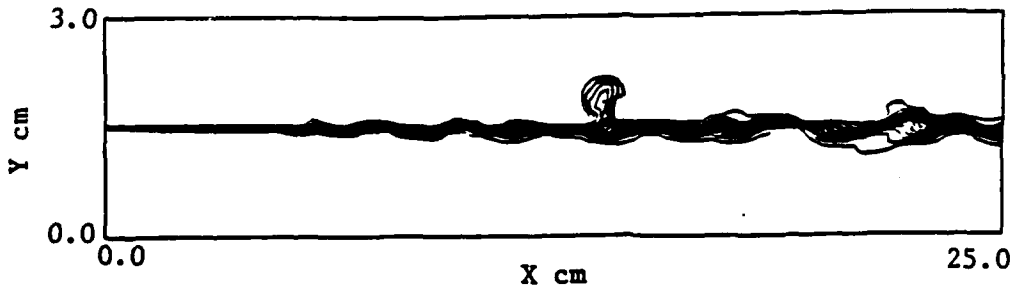


(a) $M_1 = 4.0, M_2 = 2.0, M_c = 1.0$

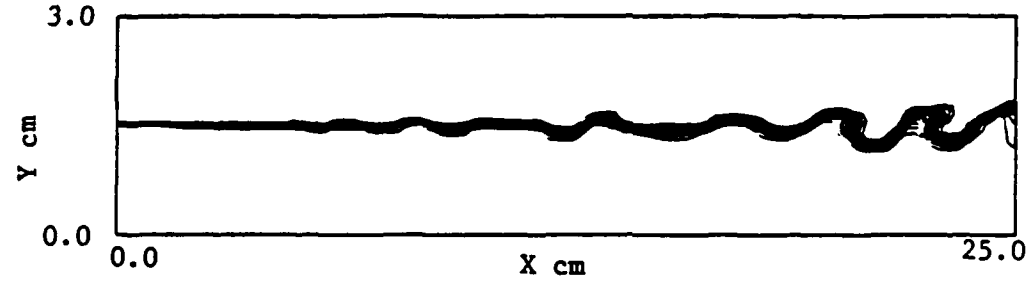


(b) $M_1 = 4.0, M_2 = 3.0, M_c = 0.5$

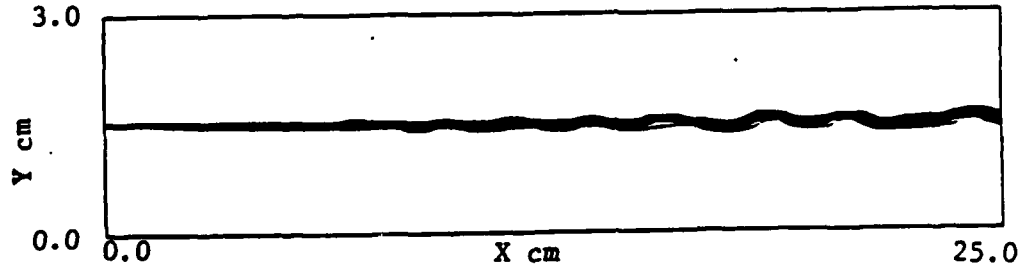


(c) $M_1 = 4.0, M_2 = 3.5, M_c = 0.25$

Figure 5. Contours of mixing ratio R from 0.01 to 0.99 at the end of time step = 4000 for $P_1 = P_2 = 1.01 \times 10^6$ dynes/cm$^2$, $\rho_1 = \rho_2 = 1.17 \times 10^{-3}$ gm/cm$^3$.

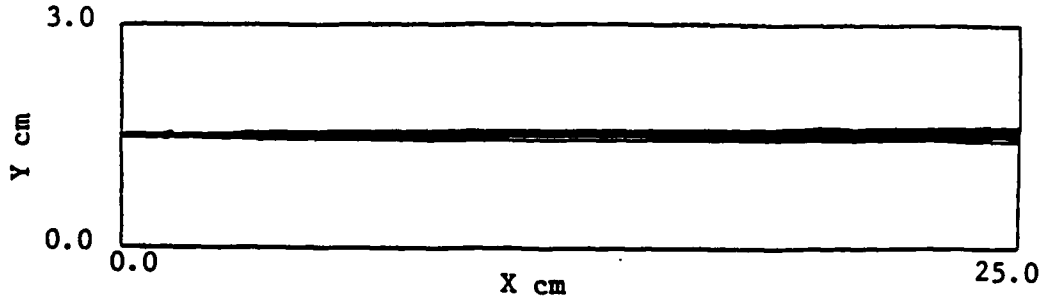


Figure 6. Contours of mixing ratio R from 0.01 to 0.99 at the end of time step = 4000. where $M_1 = 2.5$, $M_2 = 1.5$, $M_c = 0.5$, $P_1 = P_2 = 1.01 \times 10^6$ dynes/cm$^2$, $\rho_1 = \rho_2 = 1.17 \times 10^{-3}$ gm/cm$^3$

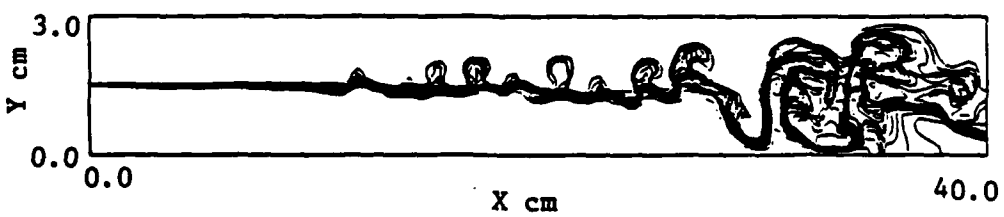


Figure 7. Contours of mixing ratio R from 0.01 to 0.99 at the end of time step = 4000 in a 40 cm x 3 cm domain. Inlet conditions are as given in Figure 2

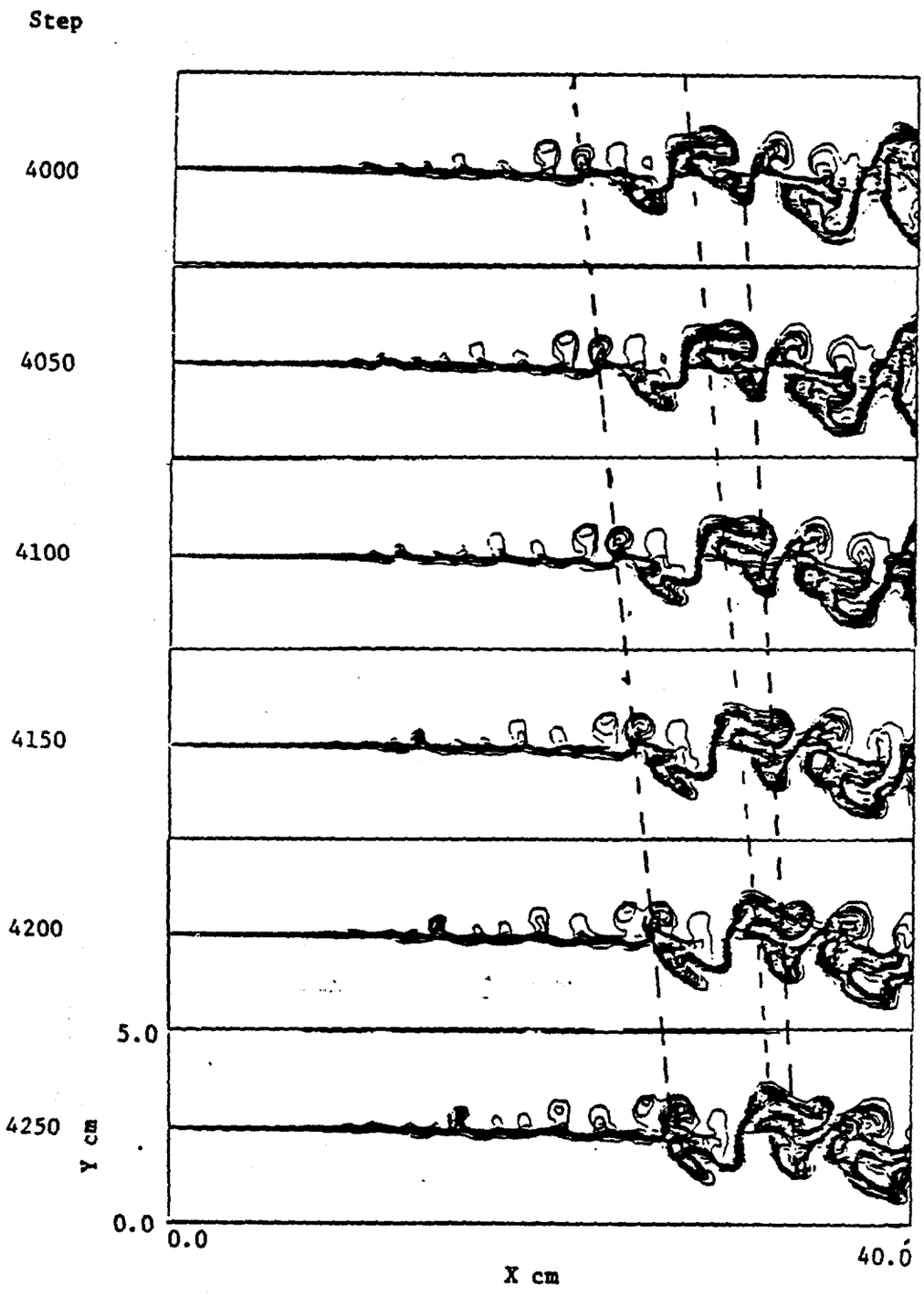


Figure 8. Contours of mixing ratio R from 0.01 to 0.99 at a sequence of time steps in a 40 cm x 5 cm domain . Inlet conditions are as given in Figure 2

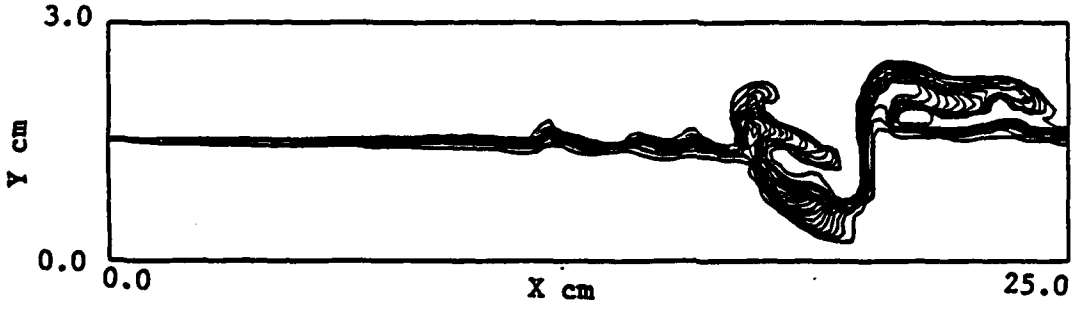


(a) 191 x 61 grid; time step = 1000

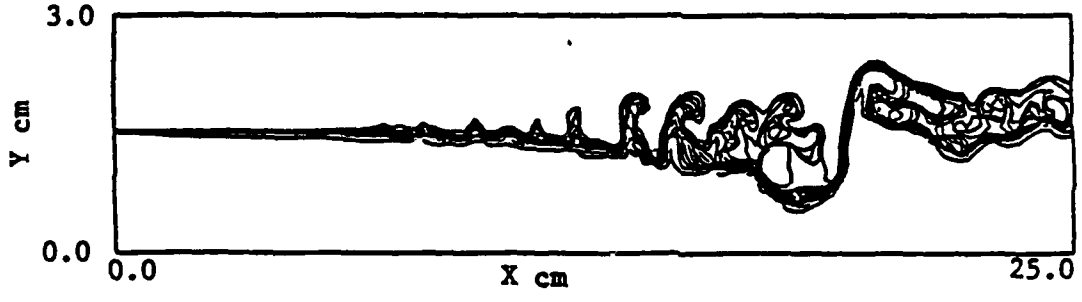


(b) 382 x 61 grid; time step = 1000

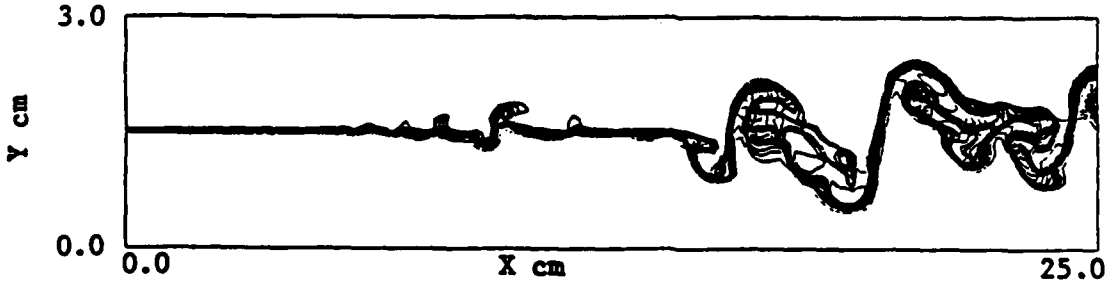


(c) 382 x 122 grid; time step = 2000

Figure 9. Contours of mixing ratio R from 0.01 to 0.99 at a given instant with different grid densities. Identical inlet velocity profile for each case.

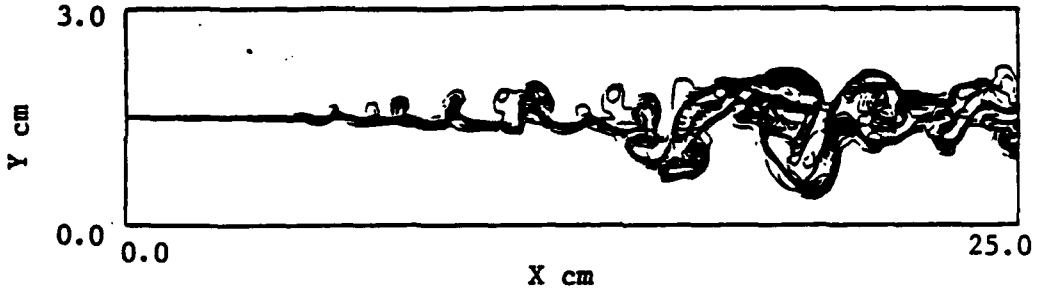


(a) 392 x 122 grid; time step = 8000

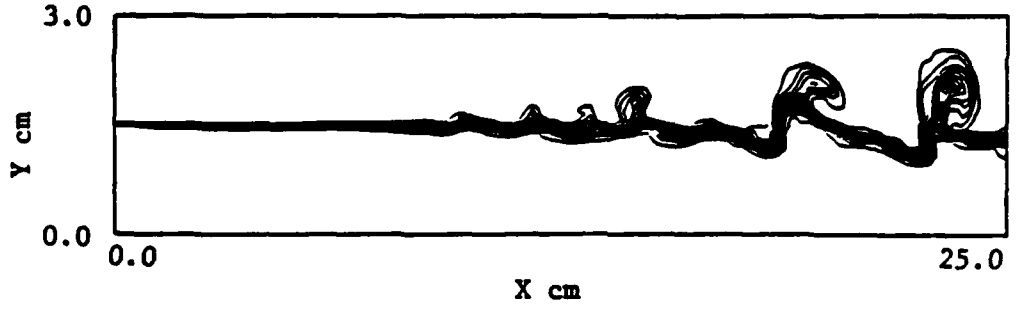


(b) 191 x 61 grid; time step = 4000

Figure 10. Contours of mixing ratio R from 0.01 to 0.99 at a given instant with different grid densities. Inlet velocity profiles are different for the two cases.

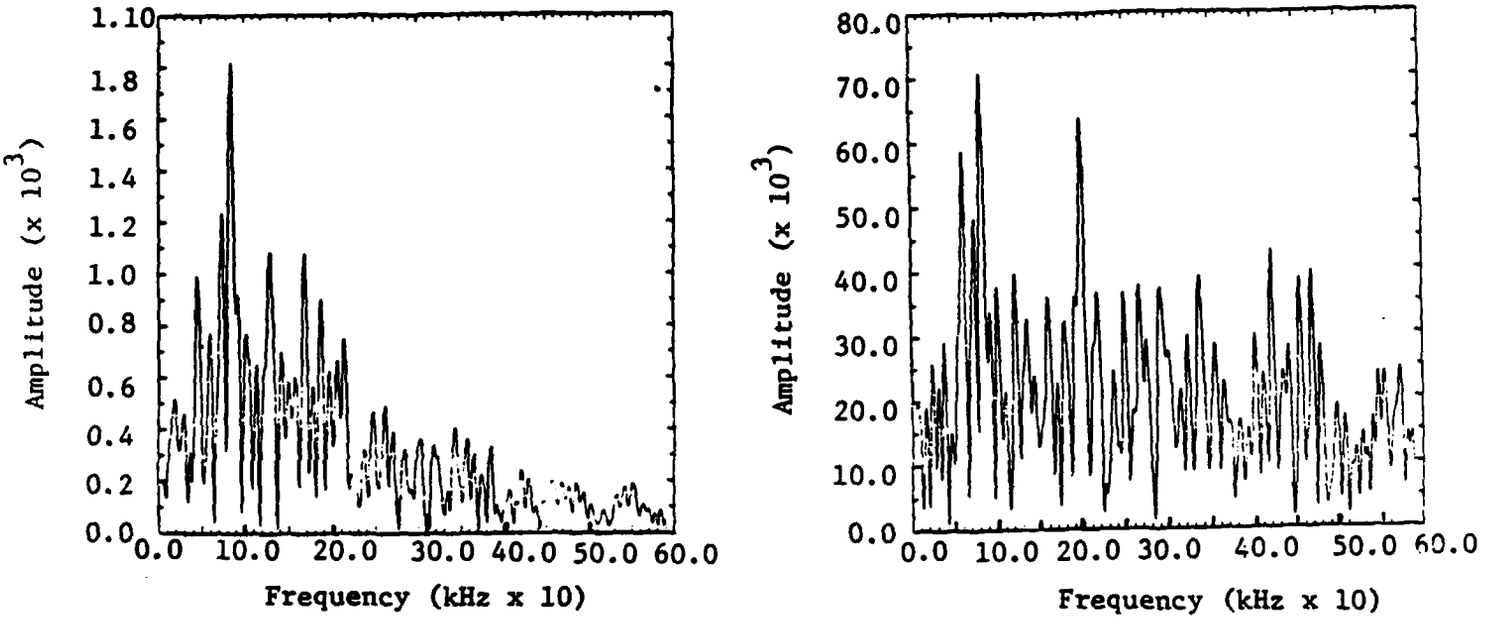


(a) Transverse velocity fluctuations

(b) Pressure fluctuations

Figure 11. Frequency spectra in the shear layer for the denser grid calculation at the location 18.75 cm (X), 2.0 cm (Y)

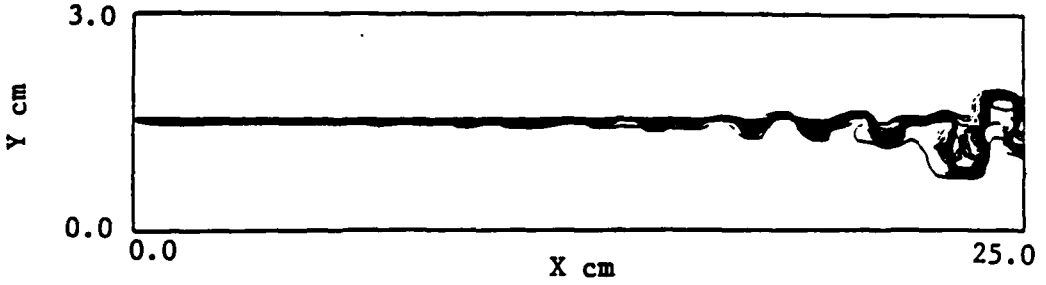


(a) $M_1 = 5.0$, $M_2 = 1.5$, $M_c = 0.67$, $P_1 = P_2 = 1.01 \times 10^6$ dynes/cm$^2$, $\rho_1 = 4.68 \times 10^{-3}$ gm/cm$^3$, $\rho_2 = 1.17 \times 10^{-3}$ gm/cm$^3$

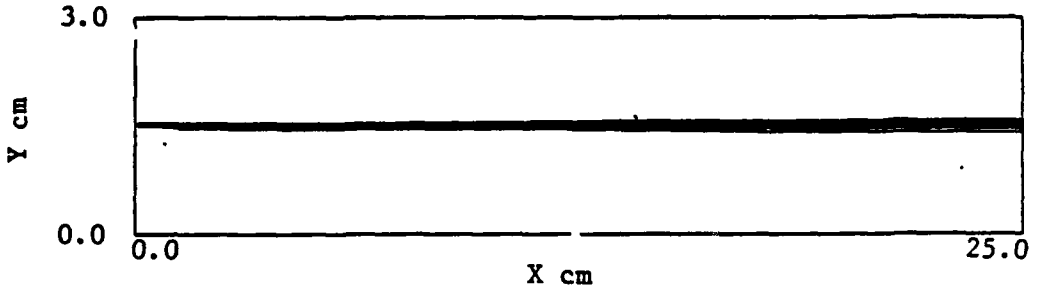


(b) $M_1 = 2.5$, $M_2 = 3.0$, $M_c = 0.67$, $P_1 = P_2 = 1.01 \times 10^6$ dynes/cm$^2$, $\rho_1 = 1.17 \times 10^{-3}$ gm/cm$^3$, $\rho_2 = 4.68 \times 10^{-3}$ gm/cm$^3$

Figure 12. Contours of mixing ratio R from 0.01 to 0.99 at a given instant (time step =4000) for the same velocity ratio but different density ratios.

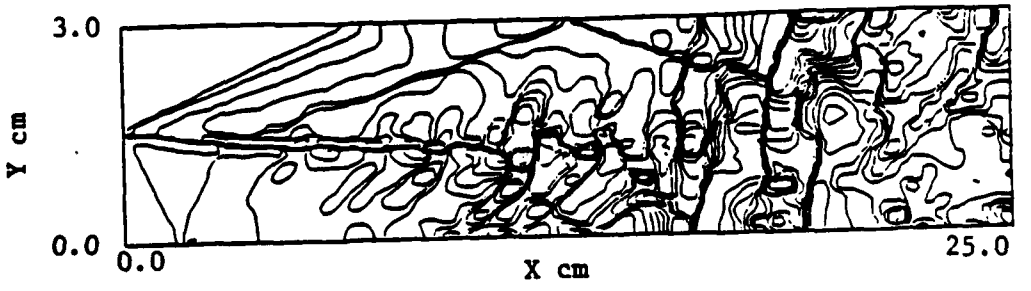


Figure 13. Density contours from $1.0 \times 10^{-3}$ to $4.0 \times 10^{-3}$ gm/cm$^3$ for an underexpanded case where $M_1 = 4.0$, $M_2 = 1.5$, $M_c = 1.36$, $P_1 = 2.02 \times 10^6$ dynes/cm$^2$, $P_2 = 1.01 \times 10^6$ dynes/cm$^2$, $\rho_1 = 2.34 \times 10^{-3}$ gm/cm$^3$ and $\rho_2 = 1.17 \times 10^{-3}$ gm/cm$^3$ at the end of time step 4000.

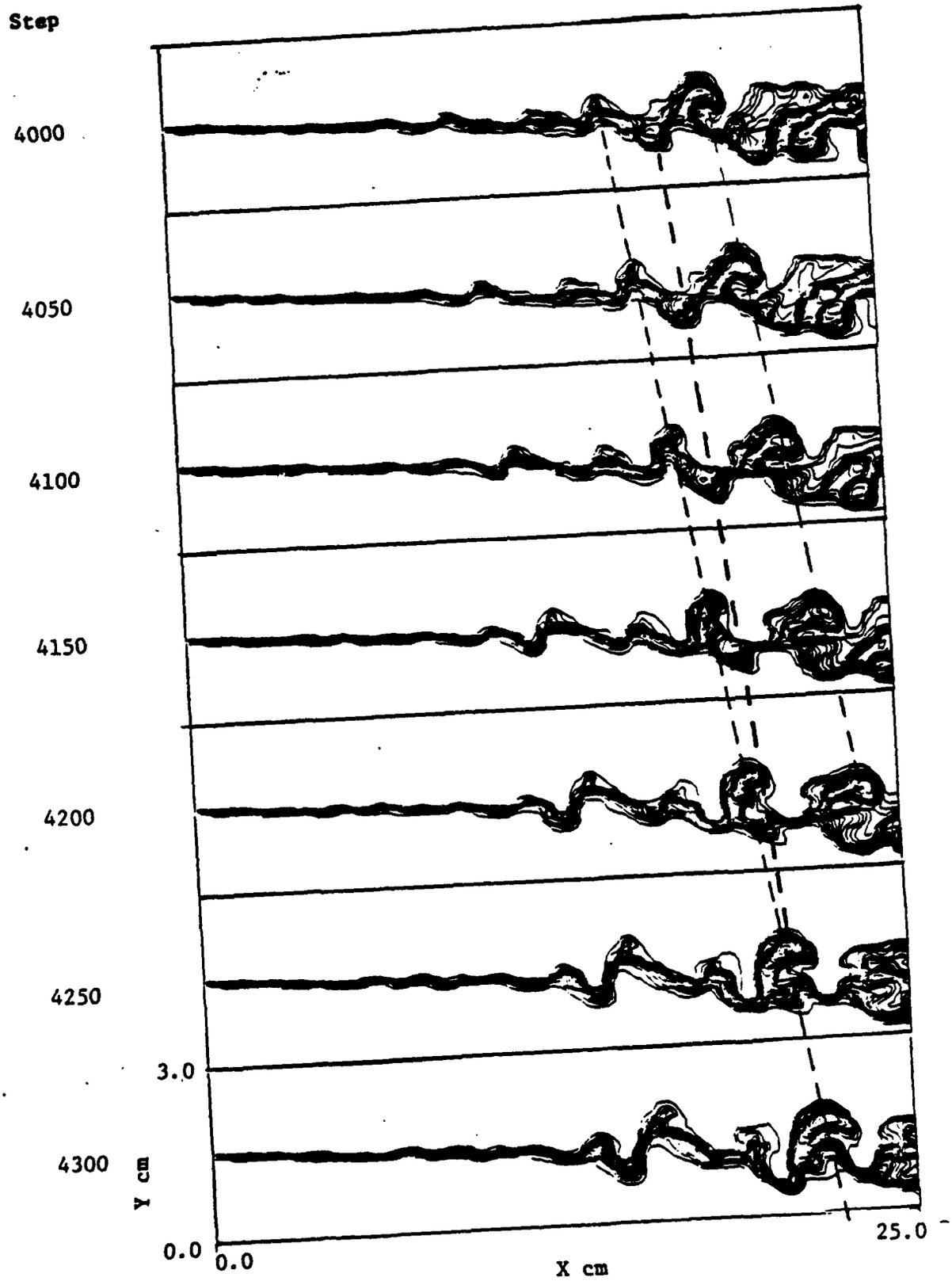


Figure 14. Contours of mixing ratio R from 0.01 to 0.99 at a sequence of time steps ( for the case shown in Figure 13)

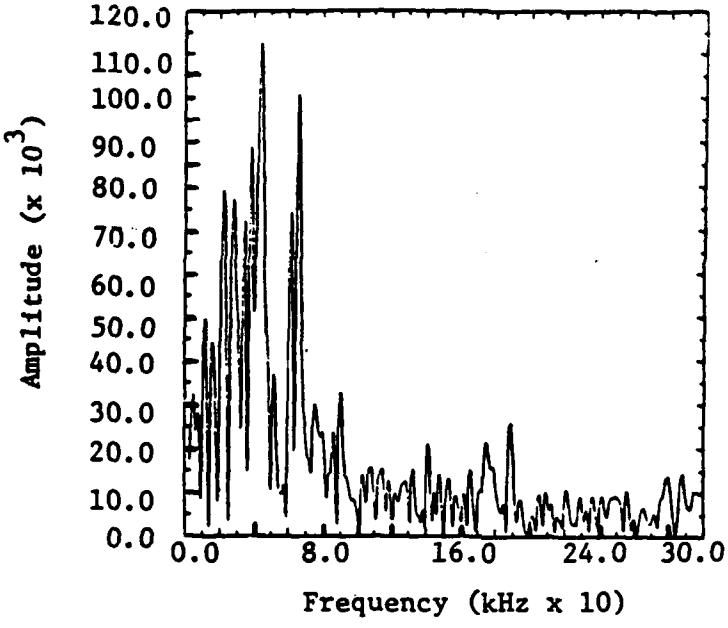


Figure 15. Frequency spectra in the shear layer for pressure fluctuations the case (shown in Figure 13) at the location 18.75 cm (X), 2.0 cm (Y)

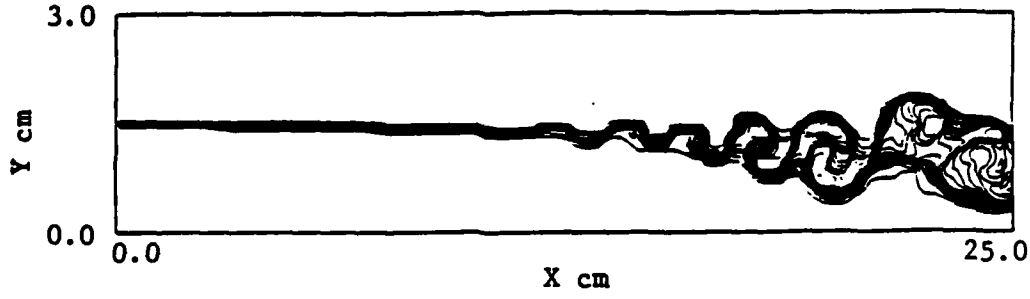


(a) Underexpanded case where $M_1 = 2.5$, $M_2 = 1.5$, $M_c = 0.633$, $P_1 = 2.02 \times 10^6$ dynes/cm$^2$, $P_2 = 1.01 \times 10^6$ dynes/cm$^2$ and $\rho_1 = 2.34 \times 10^{-3}$ gm/cm$^3$, $\rho_2 = 1.17 \times 10^{-3}$ gm/cm$^3$

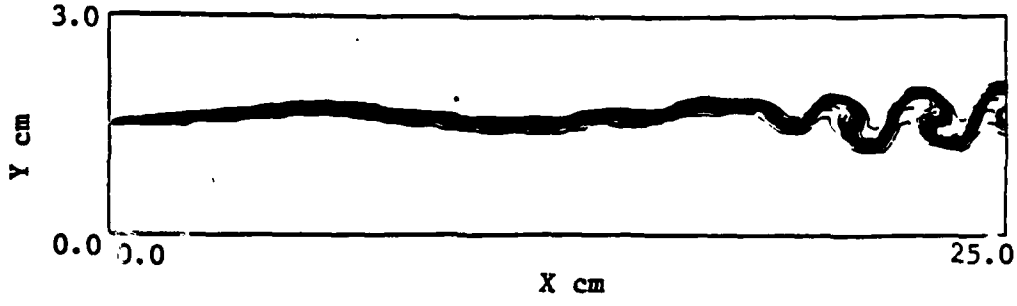


(b) Overexpanded case with $M_1 = 2.5$, $M_2 = 1.5$, $M_c = 0.369$, $P_1 = 2.02 \times 10^6$ dynes/cm$^2$, $P_2 = 1.01\ 10^6$ dynes/cm$^2$, and $\rho_1 = 2.34 \times 10^{-3}$ gm/cm$^3$, $\rho_2 = 1.17 \times 10^{-3}$ gm/cm$^3$

Figure 16. Contours of mixing ratio R from 0.01 to 0.99 at a given instant (time step =4000) for under and overexpansion.

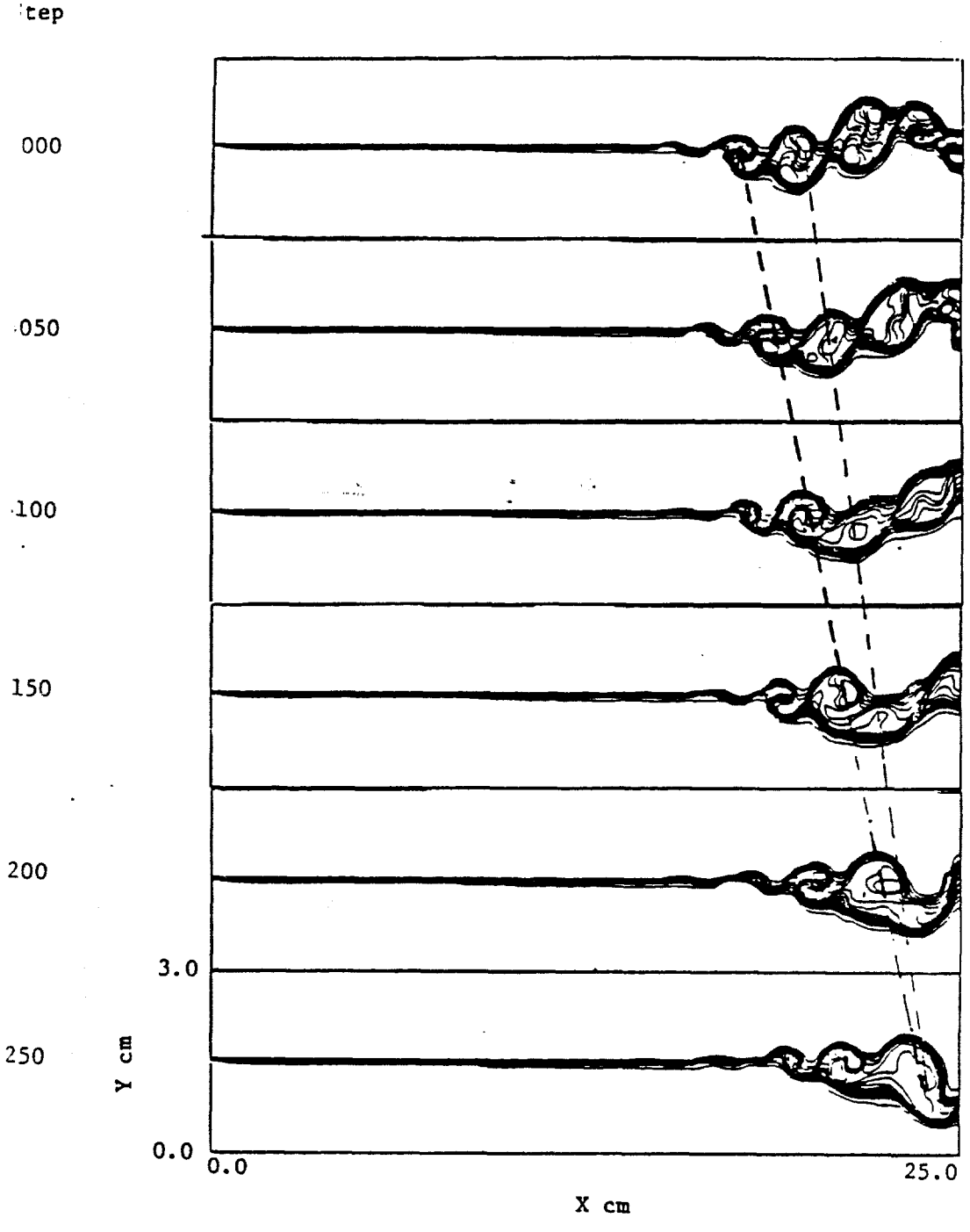


Figure 17. Contours of mixing ratio R from 0.01 to 0.99 at a sequence of time steps for a supersonic-subsonic case where $M_1 = 1.5$, $M_2 = 0.5$, $M_c = 0.5$, $P_1 = P_2 = 1.01 \times 10^6$ dynes/cm$^2$, $\rho_1 = \rho_2 = 1.17 \times 10^{-3}$ gm/cm$^3$

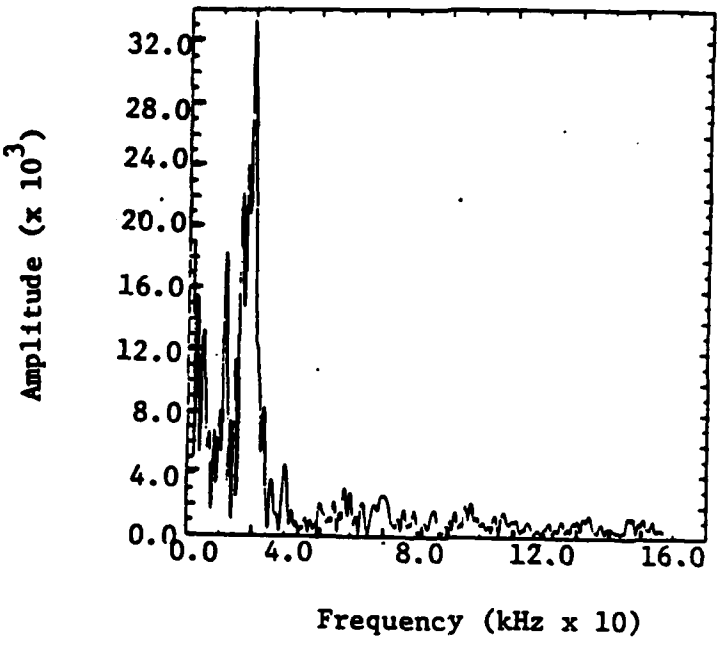


Figure 18. Frequency spectra in the shear layer for the pressure fluctuations for the case (shown in Figure 16) at the location 18.75 cm (X), 2.0 cm (Y)